Optics & Laser Technology 193 (2026) 114343

Contents lists available at ScienceDirect

Optics and Laser Technology

journal homepage: www.elsevier.com/locate/jolt

Full length article

Ablation of black-Si by (Gauss-)Bessel femtosecond laser beams

Nan Zheng[a], Hsin-Hui Huang[a], Nguyen Hoai An Le[a], Tomas Katkus[a], Haoran Mu[a], Soon Hock Ng[a], Thumula Ranaweera[a], Darius Gailevičius[b], Dominyka Stonytė[b,c,*], Saulius Juodkazis[a,b,d,**]

[a] Optical Sciences Centre, School of Science, Swinburne University of Technology, Hawthorn, Victoria 3122, Australia
[b] Laser Research Center, Physics Faculty, Vilnius University, Saulėtekio Ave. 10, 10223 Vilnius, Lithuania
[c] Direct Machining Control, UAB, Mokslininku st. 6B, 08412 Vilnius, Lithuania
[d] World Research Hub Initiative (WRHI), Institute of Science Tokyo, School of Materials and Chemical Technology, Tokyo Institute of Technology, 2-12-1, Ookayama, Meguro-ku, Tokyo 152-8550, Japan

ARTICLE INFO

Keywords:
Axicon
Black Si
Ablation
Threshold of ablation

ABSTRACT

Laser machining and modification of black-Si (b-Si) by femtosecond laser Gaussian (G-) and Gauss-Bessel (GB-) beams are compared at a wavelength of 1030 nm. The GB-beam was generated using a diffractive axicon lens and 10× demagnification optics. It was found that modification of b-Si well below (a factor ~ 50×) the single pulse ablation fluence of 0.2 J/cm^2 was possible, corresponding to ablation/melting of nano-needles. The width of modification was almost independent of pulse energy/fluence and had a width of $1/e^2$-intensity profile at the melting regime. For the GB-beam, the smallest width of laser modification at ~0.2 J/cm^2 threshold (at the center core) was close to the FWHM of the core of the GB-beam. The aspect ratio of the ablated groove on the surface of b-Si made by GB-beam was twice as large –up to 8– compared to that achievable with G-beam, and it was at a lower fluence of ~ 4 J/cm^2 (~ 50× reduction). Reflectivity of two-side nanotextured b-Si on plasma-thinned 70-μm thick Si was strongly reduced in the near-IR range, reaching transmittance > 95 % at 1.7–2.1 μm wavelengths.

1. Introduction

Black-Silicon (b-Si) is a surface-modified Si created by plasma etching. A direct laser writing with ultra-short laser pulses in selected gas mixtures can also be used to etch Si surface and form b-Si [1]. It is termed “black” because it appears visually black due to its anti-reflective property in the visible wavelength range with the surface containing a random nano-needle pattern [2–4]. The typical method for producing it involves plasma etching of silicon wafers. B-Si is produced using a standard gas-based SF_6/O_2 etching process, which is widely available in the context of standard semiconductor industrial processing [5–7]. Plasma-etched b-Si has a pattern of nano-pyramids with a typical height of 100 – 400 nm and comparable separation between adjacent pyramids preserving a crystalline nature of nano-needles [8,9]. The same results can be achieved by using gas breakdown with a femtosecond (fs) laser. However, this method tends to result in an S-doped surface [10]. Other production methods include electrochemical [11,12], stain etching [13,14], and metal-assisted chemical etching, which is favored in recent years due to its low fabrication costs and versatility in generating high aspect ratio nanostructures [15–17]. One of the applications of b-Si is in Si solar cells for the improvement of energy conversion as the reflectivity of b-Si can reach values below 1 % over the visible spectral range [18–22], other applications include photodetectors [23,24], sensors [25], and even biocidal applications of nanotextured surfaces - mechanical antibiotics [26]. The height of nano-needles is defined by the etching time, ranging from 250 nm (15 min) to 450 nm (30 min) [8].

In order to understand the energy deposition efficiency on such unusual surfaces, it is important to understand how laser machining behaves on such anti-reflective materials and acquire a clearer comprehension of the ablation, amorphization, and melting thresholds [27]. If laser ablation/cutting can utilize smaller pulse energies, then the propensity of self-focusing can be reduced. The increase in efficient energy deposition is of significant interest, especially for Si. For conventional materials, localized melting of the solid may result in volume expansion, which leads to structural failure. However, in very few cases,

* Corresponding author at: Direct Machining Control, UAB, Mokslininku st. 6B, 08412 Vilnius, Lithuania.
** Corresponding author at: Optical Sciences Centre, School of Science, Swinburne University of Technology, Hawthorn, Victoria 3122, Australia.
Email addresses: dominyka.stonyte@directmachining.com (D. Stonytė), sjuodkazis@swin.edu.au (S. Juodkazis).

https://doi.org/10.1016/j.optlastec.2025.114343
Received 9 May 2025; Received in revised form 8 November 2025; Accepted 18 November 2025
Available online 28 November 2025

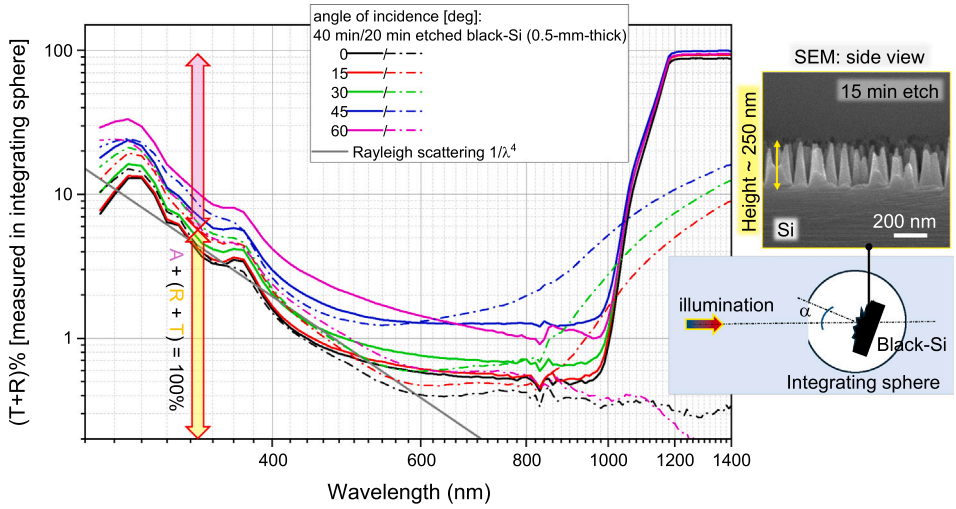

Fig. 1. Absorbance $A = 1-(R+T)$ spectra measured with integrating sphere by detection of reflectance R and transmittance T of b-Si (40 and 20 min etched; one side etched of 0.5-mm-thick Si wafer); measured with UV–vis spectrometer (Lambda 1050 UV/Vis, PerkinElmer). The right-inset shows schematics of the measurements with integrating sphere and the side-view SEM image of b-Si.

such as Si, the mass density of molten Si is higher than that of solid Si at 2.57 g/cm^3 and 2.33 g/cm^3, respectively. Other such materials include Ge, Ga, Bi, Sb [28], some compounds, such as H_2O, or some alloys, e.g., certain Ce– or Bi– based alloys [29,30]. Hence, controlled (re-)melting inside the volume of solid Si can be achieved without volume expansion and can avoid structural failure. This is promising for hyper-doping of Si by ion implantation and laser annealing [31–34]. Laser induced structural modifications in Si at high strain rates using fs-lasers showed pathway via phase transitions rather than defect generation [35] as well as observation of new high-pressure/temperature phases in the laser-affected zone [36]. Using beams with a long axial extent of the focal region, such as Bessel-like beams, offers an advantage in efficiently modifying a structured surface, such as b-Si, compared to standard Gaussian beams [37–40]. With high aspect ratio and precision, Bessel beams are becoming increasingly popular [41,42] after an early demonstration of 3D capability of fs-laser modifications of transparent materials by Bessel beams [39,43]. Bessel beams can be generated by several different approaches [40,44,45].

Here, we demonstrate the possibility for thinning Si down to tens-of-μm thickness using a dry plasma etching technique and further modifying the surface by adding b-Si nano-textures on either one or both surfaces. This texturing further reduces the reflectance of b-Si, achieving nearly 100 % transmittance for 70-μm thick double-sided b-Si sample at a wavelength of ~ 2 μm. We investigated laser structuring by ablation on the anti-reflective b-Si surfaces. It was found that surface modification through melting of the nano-needles occurs below the ablation threshold of Si (0.2 J/cm^2 [27,46]), extended to fluences by an order of magnitude smaller using Gaussian (G-) as well as Gauss-Bessel (GB-) beams. In order to compare the energy deposition of G- and GB-beams, geometrical analysis of the focusing and ablation sites was carried out. It is shown that the Liu method of ablation threshold determination [47] is applicable to the central core of the GB-beam.

2. Experimental: samples and methods

2.1. Black-Si: plasma thinning and reflectance in visible-to-IR spectral range

B-Si is produced by dry plasma etching using a simple SF_6/O_2 gas mixture [3]. Silicon thinning of a standard 300, 500 μm wafer down to tens-of-μm has become a fast and simple fabrication step. It starts with lithography performed using AZ 4562 photoresist: spin-coated at 1500 rpm for 30 s and soft-baked at 110 °C for 4–5 min. A photomask was generated using the direct-write system (Micropatterning SF100 XPRESS) and aligned with the substrate. UV exposure was conducted using an ABM UV flood light source at 450 mJ/cm^2. Development was completed in undiluted AZ 726 MIF for 12 min, with visual inspection to confirm full pattern formation. A post-development bake was ramped from 90 °C to 140 °C at 1 °C/min, held at 140 °C for 5 min, and cooled gradually. The final resist thickness was approximately 10.9 μm.

Silicon etching was carried out using SF_6 gas in a Plasmalab100 ICP380 RIE system (Oxford Instruments). Over 30 min, approximately 250 μm of silicon and 5 μm of photoresist were etched, corresponding to an estimated etch rate of ~8.3 μm/min. These values were approximated using a profilometer (Ambios XP-200), and the process remained stable with no observed plasma flickering or reflected power issues.

Fig. 1 shows the angular dependence of the absorbance of b-Si with different heights of nano-needles, corresponding to 40 min and 20 min plasma etch. For a broad spectral range of 450–1000 nm, low reflectance $R < 1$ % (large absorbance $A > 99$ %) was observed even up to angles of incidence $\theta_i \sim 30°$. Fig. 2 shows the infrared (IR) transmittance of one-sided and two-sided b-Si samples with a Si wafer thickness of ~70 μm. The texturing further increased the transmission in the IR region from 80 % to nearly 100 % for the one-sided and two-sided b-Si structures, respectively.

2.2. Geometrical parameters of the focal region produced by an axicon

Axicon is a conical lens that transforms an incoming plane wave with a Gaussian intensity distribution into a Gauss-Bessel beam with a long axial extension. Refractive and diffractive axicons are used. For the refractive axicon, the cone acts as a prism sending the incoming light into a tilted beam, making a half-cone angle γ (with optical axis). Refractive axicons are defined by the wedge angle required to form the full 180° angle at the tip of the axicon (same angle at the base of the axicon). Then, from Snell's law $\sin(\alpha+\gamma) = n_{ax}\sin\alpha$, where the refractive index of axicon $n_{ax} = 1.4$ (for silica).

The diffractive axicons are defined by the ring angle (peak-to-peak angle), which is equivalent to the full-cone angle 2γ of the refractive axicon; we used $\gamma \sim 1°$ axicon (the ring angle 2°).

Length of the central non-diffracting part of the Gauss-Bessel beam (Z_{max}) is defined by the diameter D of the beam as $Z_{max} = D/[2\sin\gamma] = 2NZ_{RB}/\pi$, where the number of rings $N = D\sin\gamma/\lambda$ and $Z_{RB} = \pi^2 k/[2k_\perp^2]$ is the Rayleigh length associated with the asymptotic width of an individual ring ($Z_{RB} = 2.656$ mm for $\lambda = 1030$ nm and $\gamma = 1°$). The component of wavevector perpendicular to propagation $k_\perp = k\sin\gamma$,

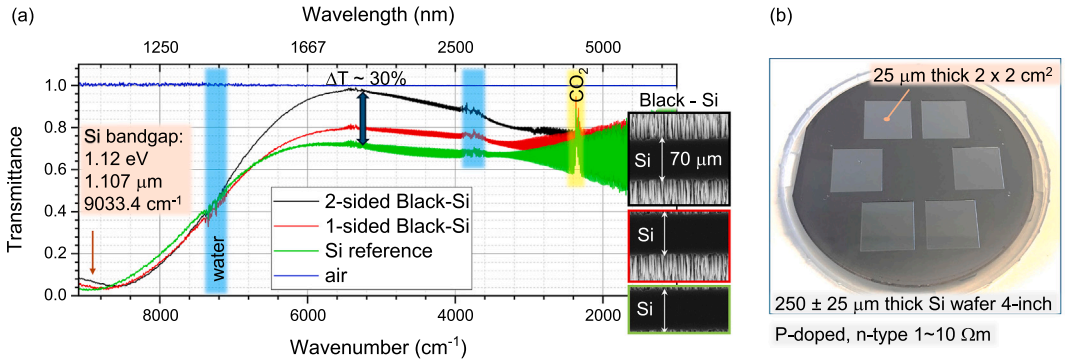

Fig. 2. (a) IR transmittance of one and two-sided b-Si (70-μm-thick; see schematic thumbnail images as insets). (b) Plasma thinned Si wafer from 250 ± 25 μm down to 25 μm at the selected regions. Direct-write mask was used to define the pattern. Silicon etching was carried out using SF_6 gas in a Plasmalab100 ICP380 reactive ion etching system (Oxford Instruments). Over a 30-minute process, approximately 250 μm of silicon and 5 μm of photoresist were etched, corresponding to an estimated silicon etch rate of ~8.3 μm/min. These values were approximated using a profilometer (Ambios XP-200).

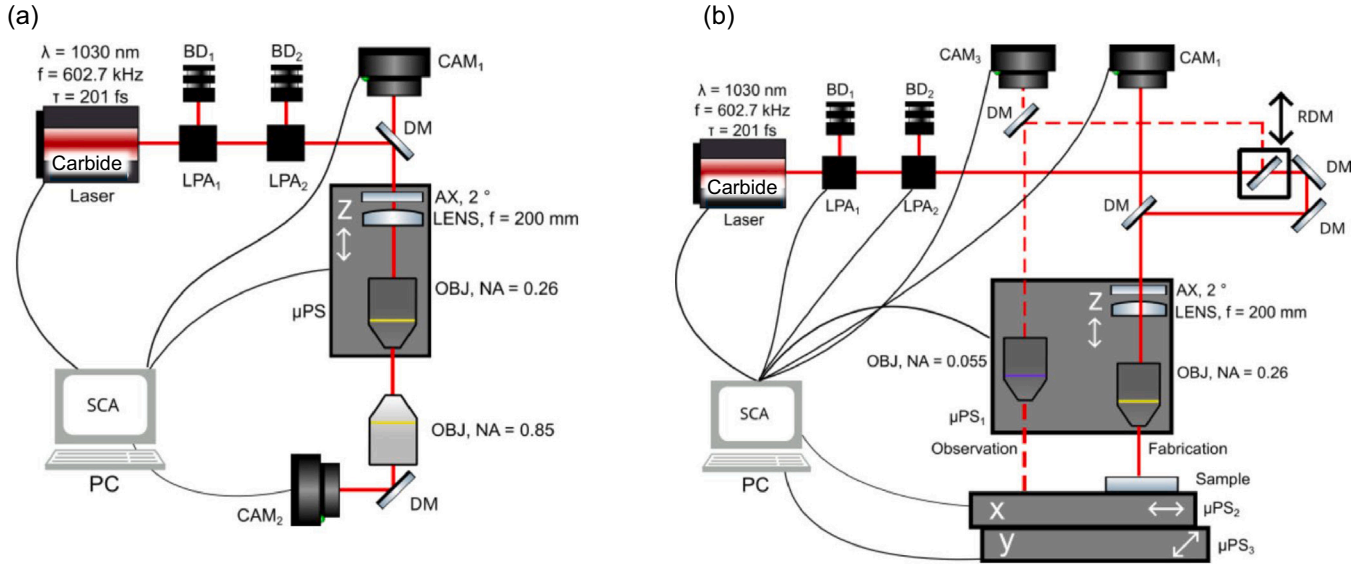

Fig. 3. Laser micro-machining setup (WOP, Lithuania) based on Carbide-40 W fs-laser (Light Conversion, Lithuania). (a) Alignment of GB-beam. (b) Fabrication and observation solution; LPA1,2 are laser power attenuators, BD1,2 - beam dumps, CAM1,2,3 – observation CCD cameras, DM – dielectric mirror, RDM – removable dielectric mirror, AX - diffractive axicon, μPS1,2,3 – micro- positioning stages and OBJ are objective lenses with numerical aperture NA; the final objective lens has f-number of $f_{\#} = F/D = 1/(2NA) = 1.92$ with focal length $F = 20$ mm and diameter of entrance pupil $D = 10.4$ mm (10× Mitutoyo Plan Apo NIR). The solid red line in (b) indicates the fabrication laser beam path, and the dashed line is the sample observation beam path. A removable dielectric mirror (RDM), mounted on a positioning stage, switches the beam paths. The observation beam path in (b) is used for G-beam machining.

where the wavevector $k = 2\pi/\lambda$. The GB-beam central spot size is typically defined as twice the first zero of the Bessel function $J_0(k_\perp \rho)$, where ρ is the radius $d_0 = 2\rho_0 = 4.816/k_\perp = 4.816/[k \sin\gamma]$ (45.2 μm for $\lambda = 1030$ nm and $\gamma = 1°$); the full width at half maximum (FWHM) central cross section is $d_0^{\mathrm{FWHM}} = 0.36\lambda/[\sin\gamma]$ (21.2 μm) [48].

For actual fabrication, these values of d_0 and Z_{max} are further downsized using a 4 f relay telescope; here we used $M_d = 10^{\times}$ demagnification which also correspondingly increased the cone angle γ' (in air for the sample position) $\sin\gamma = \sin\gamma'/M_d$ as described in the next section, Section 2.3, and shown in Fig. 3.

The energy flux associated with any ring of the Gauss-Bessel beam is equal to that of any other ring and of the central spot. The optimum central spot illumination efficiency is given by Ref. [49]:

$$\epsilon_{op} = \frac{P_{ring}}{P_{total}} = \frac{2}{\sqrt{e}} \times \frac{\lambda}{w_0 \sin\gamma} \equiv \frac{2}{\sqrt{e}} \times \frac{1}{N} \tag{1}$$

where w_0 is the $1/e^2$-radius of the Gaussian beam intensity, i.e., the diameter of the laser beam on the axicon is $D = 2w_0 = 3.5$ mm in this study. Then, the length of non-diffractive regiis on $Z_{max} = 100$ μm, the number of rings is $N = 59$, and the efficiency of central spot illumination is $\epsilon_{op} = 2$ %; for comparison, the G-beam efficiency of light collection into the focus is 100 %.

The axial intensity distribution along the GB-beam propagation (z-axis) is given [48]:

$$I_{GB}(z) = P_0 \frac{8\pi z}{\lambda} \frac{\sin^2\gamma}{w_0^2} \exp\left[-2\left(\frac{z\sin\gamma}{w_0}\right)^2\right], \tag{2}$$

where w_0 is the waist of the Gaussian beam incident on the axicon and P_0 [W] is the peak power of the Gaussian beam.

The axial intensity (Eq. 2) maximum for the diffractive axicon has two axially-shifted positions for two perpendicular polarisations. This results in two distinct peaks when a circularly polarised incident beam is used [50]. It is caused by the form birefringence with two distinct refractive indices. This was the case for our study with a circularly polarised beam ($\lambda/4$-plate was inserted into the laser output). Hence, the

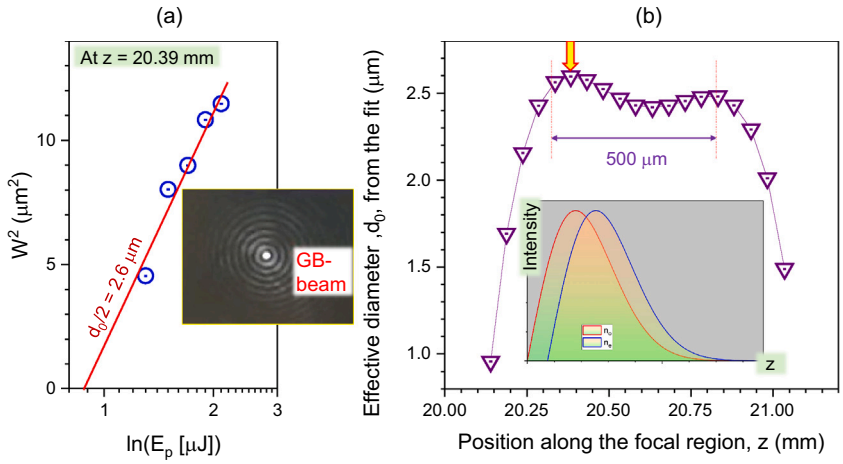

Fig. 4. Determination of the central core diameter of the GB-beam from the width (diameter), W, of ablation hole in 40-nm-thick AlOx mask on Si. (a) Diameter ablated in alumina mask $W^2(\ln(E_p))$. The *slope* of the best fit defines the radius $d_0/2 = \sqrt{slope/2}$ of the central core. The inset photo shows an image of the GB-beam at the alignment position (see Fig. 3(a) and (b)) Determination of the effective diameter d_0 along the focal region of the GB-beam. A sample of b-Si was placed at the position marked by an arrow, which corresponded to $d_0 = 5.2$ μm. The axial extent of the non-diffracting region was ~ 500 μm. Circularly polarised light was used for illumination of the diffractive axicon, which caused doubling of the characteristic axial GB-beam profile (Eq. 2) shown in the center-inset for the ordinary and extraordinary refractive indices of the form birefringent structure of diffractive axicon $n_{o,e}$.

final 10× down-sized GB-beam had double length of ~ 500 μm; for one polarisation, $Z_{max}/10 \approx 266$ μm is expected for the used setup/geometry (see Section 2.3 and Fig. 4).

2.3. Laser micro-machining setup

For the GB-beam we used Workshop of Photonics (WOP) fs-fab station with a Yb:KGW laser system Carbide (Light Conversion), which has an output power of 40 W, fundamental harmonic wavelength 1030 nm, repetition rate of 602.7 kHz, pulse duration of 201 fs (Fig. 3). A diffractive axicon with a ring angle of $2\gamma = 2°$ was used (Holo OR). A combination of an $f = 200$ mm lens (placed close to the axicon) with an objective lens MPlan APO NIR 10× Mitutoyo, $NA = 0.26$ and $f = 20$ mm was used to form a 4 f system for the imaging and down-scaling 10 times the intensity distribution on the sample (Fig. 3(b)). Observation and inspection were carried out using MPlanApoNIR 2× $NA = 0.055$.

In a separate experiment, determination of the ablation threshold at the central core of the GB-beam was carried out using a 40-nm-thick AlOx mask on Si wafer surface and applying the standard Liu method developed for G-beams [47]. Ablation of AlOx mask creates a very distinct hole and is useful for determining the central focal spot of GB-beam at the fabrication position; such masks were used in the fabrication of light trapping surface of Si solar cells [51]. The diameter of the ablated hole in the nano-thin alumina mask vs fs-pulse energy was plotted as $W^2(\ln[E_p])$ for different positions along the non-diffracting zone using the same objective lenses and setup described above (Fig. 4(a)). The sample position for fs-laser machining was determined by the axial location, where the steepest dependence of the diameter of the ablated hole on the pulse energy was observed (Fig. 4(a)). The corresponding threshold pulse energy was $E_p^{(th)} \approx 900$ nJ (entire pulse) and the effective beam waist for the ablation at the center core was $d_0/2 = 2.6$ μm. The estimate of an average fluence per central core (per pulse) for the used efficiency $\epsilon_{op} = 1$ % of GB-beam (1 % is considered instead of 2 % due to circularly polarised beam and separation of the intensity maxima into two peaks for two perpendicular polarisations). One finds $F_p^{(th)} = \epsilon_{op} E_p^{(th)}/[\pi(d_0/2)^2] = 0.043$ J/cm^2. The difference of diameters at the first-zero and FWHM of the GB-beam for the used geometry is $d_0/d_0^{\mathrm{FWHM}} = 2.13$. Then the energy in the central core per d_0^{FWHM} for the ablation threshold corresponds to the threshold fluence $F_p^{(th)} \times 2.13^2 = 0.2$ J/cm^2, which exactly matches that for Si. The $d_0^{\mathrm{FWHM}} = d_0/2.13 = 5.2/2.13 = 2.44$ μm.

The analysis of focusing using geometry outlined above for diffractive axicon $\gamma = 1°$ and 10× demagnification, corresponds to the center core energy of 1 % of that incident, which is focused onto a spot of $d_0^{\mathrm{FWHM}} = 2.44$ μm. These conditions will be used for analysis of fs-laser modification (melting and ablation) of b-Si and determination of the fluence at the center core (defined by d_0^{FWHM}).

3. Results

Ablation and energy deposition onto b-Si were investigated using 1030 nm/200 fs pulses at different spacings between pulses in a linear scan. Gaussian and Gauss-Bessel fs-laser beams were used with comparable size of the central focal spot: 2.8 μm (Gaussian) and 2.6 μm (center-core Gauss-Bessel) diameters.

3.1. Gaussian beam

The diameter of the Gaussian (G-)beam can be estimated as $d_G = 1.22\lambda/NA$ for the objective lens of numerical aperture; $NA = 0.45$ in this study. It is the diameter of the Airy disk, i.e., between two minima (zero intensity) in cross section for a plane wave focusing limited only by diffraction. In terms of energy under the envelope of the Gaussian beam intensity profile (86.5 %) and within the Airy-disk for the plane wave (84 %), both are very similar.

Fig. 5 shows a typical sample with lines laser ablated at different pulse energies and spacing between adjacent irradiation spots. A sample of b-Si was cleaved across the line pattern for the side view observation of the ablation depth D and width W (Fig. 5(a)). At very low pulse fluence, well below the ablation threshold of Si 0.2 J/cm^2 [46], surface modification of b-Si had clear imprint of melted nano-needles with discernible rim with diameter of 2.8 μm, which matched the focal spot size for the used $NA = 0.45$ objective lens $2r_G = 1.22\lambda/NA = 2.8$ μm. This diameter was used for the determination of the average pulse fluence $F_p = E_p/(\pi r_G)^2$; the peak fluence and intensity are larger by a factor of 2 than the average, assuming the Gaussian pulse.

The dependence of ablation/modification width on the pulse fluence is presented as $W^2(\ln[F_p])$ in Fig. 6(a). Log-log presentation is chosen to better reveal the change in the slope, which is linked to the mechanism of the modification. This is similar to the Lin-log presentation of the same dependence known as the Liu method [47]. For the largest separation between pulses close to the focal diameter, the threshold of modification is close to 0.2 J/cm^2, which is the expected threshold for

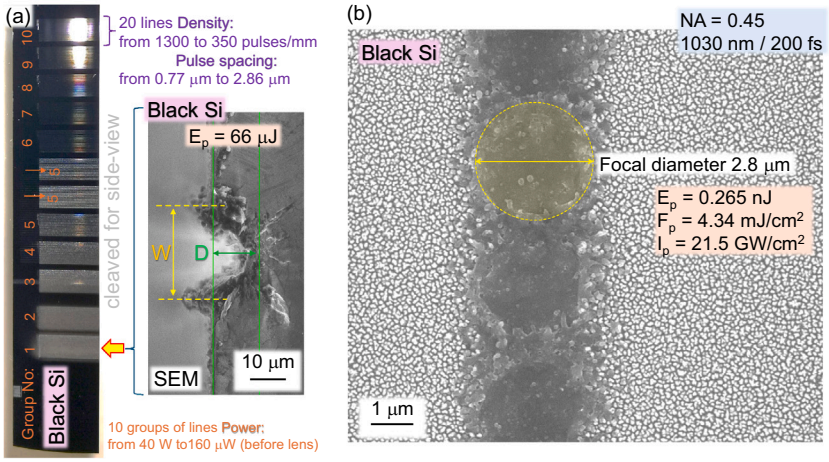

Fig. 5. Black-Si ablation by Gaussian fs-laser beam. (a) Photo of fs-laser machined regions (left) and side view SEM image of ablation crater (right). Lines were ablated at different conditions shown in groups No. 1–10. The cleaved sample across the lines was observed by SEM for a side-view to determine the depth and width of the individual grooves. (b) SEM image of laser-ablated sites with distinct imprints of 2.8 μm focal spots on the surface of b-Si. The diffraction limit $1.22\lambda/NA = 2.8$ μm for $\lambda = 1030$ nm wavelength and objective lens of numerical aperture $NA = 0.45$.

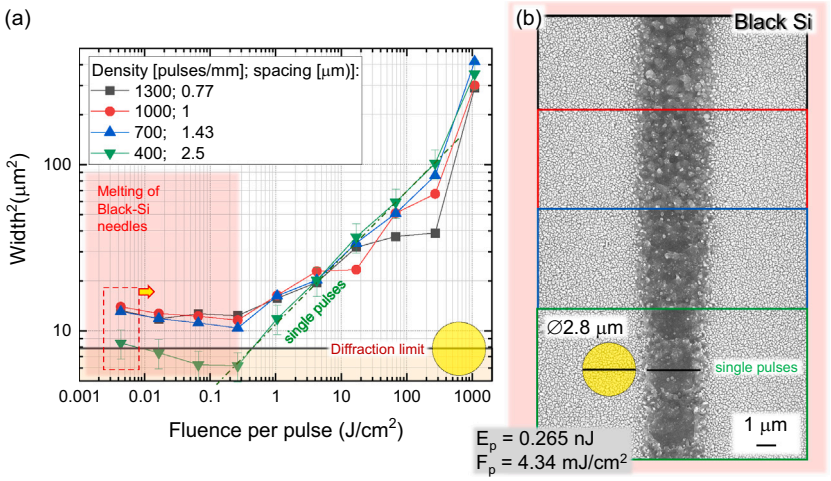

Fig. 6. Ablation by a Gaussian beam. (a) The width vs. single pulse fluence $W^2(F_p)$ for different pulse densities (pulse-to-pulse separation/spacing) ranging from just separated pulses to strongly overlapped. Error bars for single pulse data are 20 %. (b) SEM images of the lowest fluence modification made by remelting the b-Si surface.

Si ablation. However, at much lower fluence ~ 4 mJ/cm^2 by a factor of 50, a clear surface modification was still observed. There was a tendency of saturation of the width W at a low-fluence region and even slight increase at the lowest values, however, it was within the experimental error. Apparently, a melting of a very tip of b-Si needles, or larger volume are sensitively recognized in SEM imaging especially due to the multi-pulse accumulation case. The structural surface modification at sub-0.2 J/cm^2 fluences is linked to the melting of nano-needles of b-Si and was lower as observed on flat Si [27].

There was almost no change in the width of melt-modification (Fig. 6(b)). This confirms that direct energy deposition occurred only over the focal spot and the lateral heat diffusional spread was negligible, as shown in Fig. 6(b). Interestingly, at the maximal used fluence, the width was increasing at a steeper rate vs F_p, departing from the expected linear dependence of the Liu plot. This could be linked to the better energy deposition at the surface of b-Si due to low reflectance. Fig. 7 shows the evolution of the depth and aspect ratio of the ablated groove. For the low pulse overlap, close to single pulse ablation conditions, the threshold fluence projects to the expected 0.2 J/cm^2 for Si.

3.2. Gauss-Bessel beam

To calculate the energy, fluence and irradiance (intensity) per pulse at the center core of the Gauss-Bessel (GB-)beam is not trivial, as in the case of the Gaussian beam, since the energy of the GB-beam is spread over the number of rings, which carry the same energy and converge onto optical axis at different locations along the propagation. Moreover, for the diffractive axicon, there are two axially shifted intensity distributions (Eq. 2) for two perpendicular polarisations [50]. This reduces energy distribution per ring by half. It is noteworthy that the Liu method can be used for different non-Gaussian beam shapes [52].

We adopted the established Liu method [47] for G-beam to measure the effective diameter of the focal spot at different locations along the focal region (non-diffractive zone of GB-beam) as described in Section 2.3. The test sample for measurement of ablated diameter vs the pulse energy was a 40-nm-thick AlOx coated mask on Si. It was placed at different positions of ~ 1 mm long focal region of the GB-beam using the same axicon and focusing conditions.

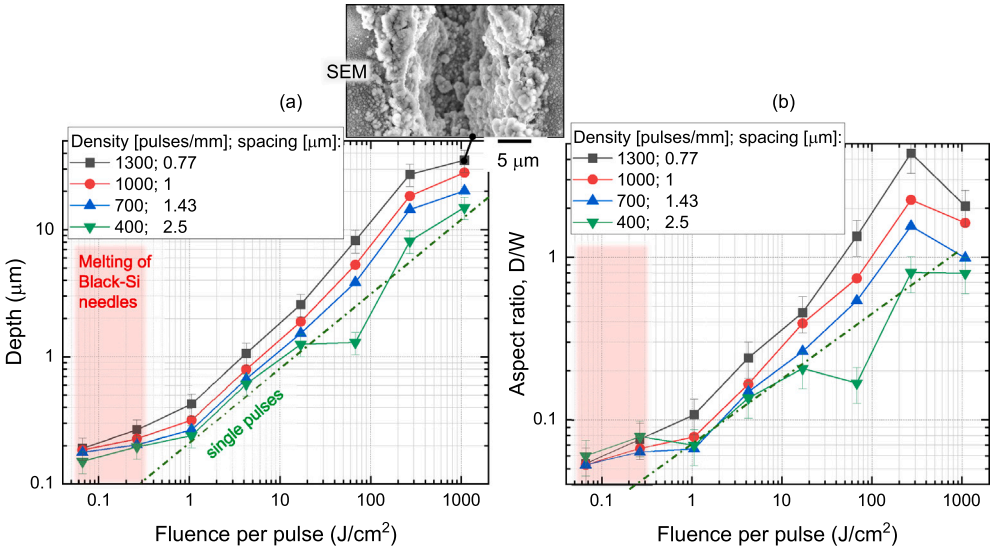

Fig. 7. Ablation by a Gaussian beam. (a) Depth vs. fluence per pulse. The top inset shows a SEM image of high-fluence, small spacing ablation; error bars are 20 %. (b) The aspect ratio vs. fluence per pulse, error bars are 25 %.

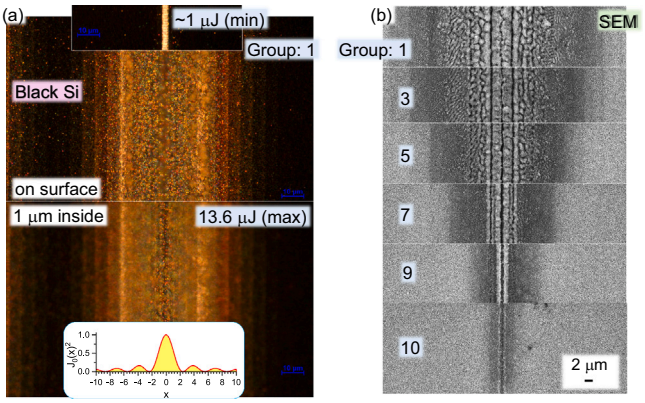

Fig. 8. Black-Si ablation by Gauss-Bessel beam. (a) Dark-field image (with $NA = 0.9$ objective lens) of ablated line at high pulse energy E_p. The top inset shows the lowest pulse energy ablated line, and the bottom inset shows the Bessel function where $x = k_{\perp}\rho$. (b) SEM top-view images of ablated lines at different pulse energies (by group number). Ripples at off-center locations of GB-beam show that polarisation was linear (or elliptical) rather than circular, which is aimed at the center core.

According to the Liu method [47] for the G-beam, the diameters, W, of the ablated pits (or width of the ablated line) on the sample at different pulse energies are determined. The intercept of a linear fit of $W^2[\ln(E_p)]$ corresponds to a threshold pulse energy E_{th} (also threshold fluence $F_{th} = E_{th}/(\pi w_0^2)$) while the *slope* corresponds to $2w_0^2$:

$$W^2 = 2w_0^2 \ln(E_p/E_{th}). \tag{3}$$

The waist (radius) of the Gaussian beam at the focus is $w_0 = \sqrt{slope/2}$ (Eq. 3).

We verified this experimental procedure of focal diameter determination using ablation of AlOx mask on Si using GB-beam for the center-core ablation/modification as described in Section 2.3 and shown in Fig. 4. It was determined that the ablation threshold of Si 0.2 J/cm^2 corresponds to the energy at the center core over its FWHM cross section. Also, as in the case of G-beam, the diameter of the center core (energy deposition) is determined from the low pulse energies.

Typical patterns of GB-beam ablated b-Si are shown in Fig. 8. The dark-field optical image in (a) shows a pattern at high energy/fluence at the surface of the sample and 1 μm depth. SEM images at the same high fluence and down to low energy E_p when only the center core is discernible are overlaid in (b). Counterintuitively, the width of the central opening was narrower for the high E_p. This is caused by the formation of a high-aspect-ratio central groove and redeposition/oxidation around the center core. For this particular reason, analysis by Eq. (3) cannot be applied for the b-Si; however, it was verified for the mask hole ablation of alumina-coated Si as described previously (Section 2.3).

At the lowest pulse energies, a clear molten b-Si surface is observed with clearly discernible 2.6 μm diameter (Fig. 9). It is very close to the expected FWHM diameter of 2.44 μm as determined from the geometrical conditions and focusing (Section 2.3). This diameter was used to calculate pulse fluence at the center core as previously validated in the adaptation of the Liu method. The sample position for the alumina mask ablation on Si and b-Si was the same as for all the beam delivery optics.

Fig. 10 shows the depth and aspect ratio evolution with fluence per center core at different pulse-to-pulse spacings. Close to linear dependence was observed over the span of one order of magnitude in F_p (per pulse per center core). Since the large surface area is affected, the determination of width W had a large uncertainty (obvious also from Fig. 8(b)). This is why some data points are excluded from the aspect ratio plot in (b). A formidable high aspect ratio > 5 was observed for the center fluence > 2.5 J/cm^2. A deep central ablation groove was formed under those conditions, and the imprint of up to 3 rings was present

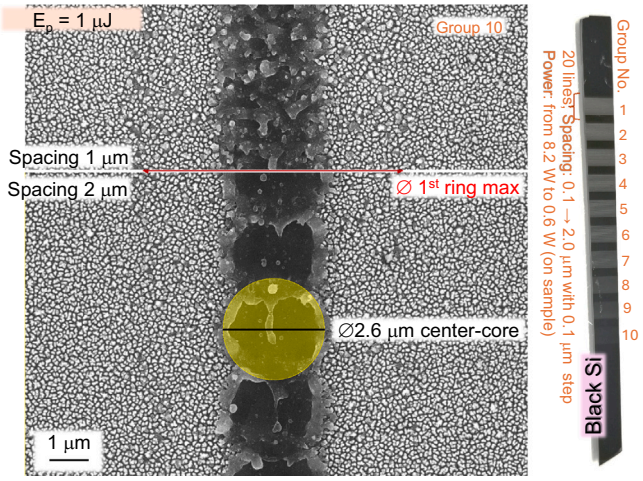

Fig. 9. SEM image of b-Si ablated by Gauss-Bessel beam at lowest pulse energy. It was used to determine the diameter of the center core. The right-side inset photo shows the b-Si sample cleaved across all the patterns recorded under different conditions for the side-view imaging of the depth and width; groups of lines No. 1–10. The position of the first ring maximum is barely recognisable (marked by a red arrow), however, it was not possible to quantify such modification in terms of ablation width nor depth.

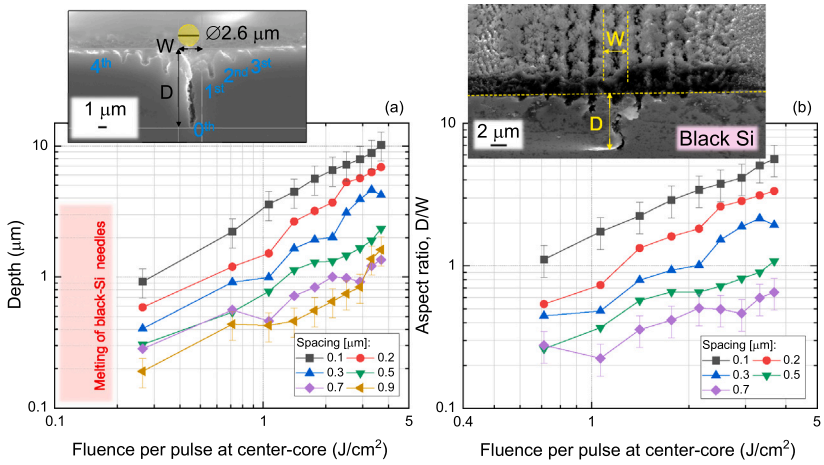

Fig. 10. Ablation by a Gauss-Bessel beam. The depth D (a) and aspect ratio W/D vs effective fluence per center-core $d_0 = 2.6$ μm diameter. The fluence was calculated as E_p over the area of diameter d_0 (experimentally observed at lowest fluences); a factor of 1 % was used for energy redistribution into the center core as determined in Section 2.3. Error bars are 25 %.

on the surface. Apparently, the energy deposition has a larger aspect ratio as compared with the G-beam case. This can be facilitated by the anti-reflective property of b-Si, deeper optical light penetration due to 1030 nm wavelength being close to the bandgap of Si.

4. Discussion

It is shown here that the Liu methodology of determination of ablation threshold, originally demonstrated for G-beams, is applicable to the center core GB-beams. When the FWHM of the central core was taken as the diameter of the energy deposition, the efficiency of energy at the center beam was calculated using ideal Bessel beam properties under the employed focusing conditions. This is useful for comparing G- and GB-beam laser machining, at least at the semi-quantitative level. Exact Bessel-like beam geometry and properties are affected by focusing, filling/clipping at the entrance apertures, and demagnification telescope alignment, in addition to the type of optical element, refractive, diffractive, metasurface, and the quality, which determines phase imperfections.

Anti-reflective property of b-Si allowed very precise control of energy deposition with clear accumulation effect revealed in Fig. 6: the smaller spacing, i.e., the larger pulse overlap, the slope of W^2 vs F_p dependence is less steep, especially towards smaller fluencies. Apparently, the cumulative effect of irradiation is enhancing energy deposition and remelting of nano-needles. Larger droplets at stronger overlap signify higher surface temperatures over larger volumes, which was able to minimize surface area by forming spheroidal droplets. Such controlled melting has potential for surface doping of materials when b-Si is coated by other elements which are potential dopants for n- or p-type conductivity as well as formation of intra-band states for IR sensors [53]. Black-Si produced by plasma etch has a surface with native oxide similar to the flat Si with detectable F presence [9]. This makes doping and remelting of nano-needles with surface deposited dopants a promising avenue for tailoring surface properties and chemistry.

We can put forward a conjecture that light localisation between nano-needles and at the interface Si-air with large E-field components normal-to-the-interface contributes to energy deposition. Inducing defects which enhance absorption of subsequent pulses, driving energy deposition onto this antireflective surface. Indeed, it corresponds to the p-polarisation rather than s-polarisation and has lower reflectance (see simulations in Ref. [54]).

4.1. Ablation threshold of black-Si

Easily recognisable surface modification is observed at a much lower threshold than expected for Si ablation at 0.2 J/cm^2 per pulse (for optically flat Si) [46]. Ablation thresholds of metals (m) and dielectrics/semiconductors (d) is related to ionisation and are estimated from the energy deposition which exceeds the cumulative binding energy (enthalpy of vaporisation) ϵ_b and electron work function (for metals) w_e or ϵ_b and ionisation potential J_i for dielectrics and semiconductors [55]:

$$F_{th}^{(m)} = \frac{3}{8}(\epsilon_b + w_e)\frac{\lambda n_e}{2\pi}, \qquad F_{th}^{(d)} = \frac{3}{4}(\epsilon_b + J_i)\frac{l_s^* n_e}{A}. \tag{4}$$

where $l_s^* = c/(\omega\kappa) \equiv \lambda/(2\pi\kappa)$ is the absorption depth (the skin depth for the E field) in the plasma with electron density n_e and refractive index $n^* = n + i\kappa$ with c and ω being the speed and cyclic frequency of light, respectively; A is the absorption coefficient (for good metals $A \approx 2\omega l_s^*/c$). At high intensity, the pulse can exceed the ionization threshold and the first ionization is completed (before the end of the pulse), at which the number density of free electrons saturates at the level $n_e \approx n_a$, where n_a is the number density of atoms in the target material.

For ablation of dielectrics and semiconductors, which are ionized during the fs-pulse, a metal-like reflective plasma has $A \approx 0.5$; i.e., half of the light is absorbed by the strongly excited material. The exact absorbed portion $A = 1-R$, where R accounts for the reflected portion of the laser pulse, can be precisely calculated from the refractive index $n^* \equiv n + i\kappa$ as $A = 4\,n/[(n+1)^2 + \kappa^2]$. The ablation threshold of metals (Eq. 4) scales with wavelength $F_{th}^{(m)} \propto \lambda$ [55]. Eq. (4) is based on the required energy budget to evaporate material ϵ_b and to ionize it: w_e for metals and J_i for dielectrics. These thresholds are confirmed by experiments for metals and dielectrics [55].

For unperturbed Si, $\epsilon_b = 383$ kJ/mol, the first ionisation potential $J_i = 786.52$ kJ/mol (8.152 eV per atom) and typical $n^* = 3.5 + i0.01$ corresponding to a low doping Si $n_e = 1{\times}10^{16}$ cm^{-3} (or resistivity $\sim 1\ \Omega$.cm); the skin depth reciprocal to the absorption coefficient (for intensity E^2) $l_s = 1/\alpha = (4\pi\kappa/\lambda)^{-1} = 8.2\ \mu$m; $\alpha = 1.22 \times 10^3$ cm^{-1}, $A = 69.1$ % at $\lambda = 1030$ nm wavelength. Upon fs-laser irradiation, the electron density approaches the critical plasma density $n_{cr} = \omega^2\varepsilon_0 m_e^*/e^2$ at which the real part of permittivity decreases and the imaginary part increases $\varepsilon^* = \varepsilon_1 + i\varepsilon_2$. Under such conditions, the most efficient energy deposition takes place (energy per volume), and dielectric breakdown follows. For $\lambda = 1030$ nm, $n_{cr} = 1.05 \times 10^{21}$ cm^{-3}, where ε_0 is the permittivity of free space, m_e^* is the effective mass of electron. The dielectric breakdown is defined by the real part of permittivity becoming zero: $\varepsilon_1 = (n^2 - \kappa^2) \equiv 0$ and $n = \kappa$; $\varepsilon_2 = 2\,n\kappa$ defines absorption losses of light in the sample. Assuming that photo-excited Si approaches $n = \kappa = 0.2$, one finds $A = 54.1$ % and for the plasma density close to critical $n_e \approx n_{cr}$, at which the ablation threshold of Si becomes $F_{th}^{\mathrm{Si}} = 0.232$ J/cm^2 (Eq. 4); for these conditions $l_s \equiv l_s^*/2 = 410$ nm (close to the height of b-Si nano-needles [8]) $\alpha = 2.44 \times 10^4$ cm^{-1}. The threshold is close to the experimentally observed ablation threshold on flat Si by ultra-short laser pulses 0.2 J/cm^2 [46].

When Si is turned into black-Si, the material properties ϵ_b and J_i remain the same, however, the absorption coefficient A is effectively increased due to the reduced reflectivity. Indeed, when there is no transmission $T = 0$ (an optically thick sample), the energy conservation $A + R + T = 1$ demands $A = 1 - R$. This can be interpreted as a reduced ablation threshold expected for the anti-reflective surface and observed experimentally in this study (Fig. 6).

Ablation (removal of material) takes place when the pool of energy absorbed by electrons transfers it to the lattice and heats it above the evaporation conditions (the binding energy). The temperature of electrons in the skin depth is $T_e = (1 - R)F_p/(l_s c_e n_a)$ [55], where F_p is the fluence per pulse, $c_e \sim 3/2$ is the electron specific heat, which acquires the value of 3/2 of the ideal gas after full ionization of material, and n_a is the atomic number density of the material (for Si $n_0 = \rho_{Si} N_{av}/M_{Si} = 4.99 \times 10^{22}$ cm^{-3}, here the mass density $\rho_{Si} = 2.33$ g/cm^3, molar mass $M_{Si} = 28.08$ g and N_{av} is the Avogadro number). This energy deposited into electrons acts as an energy reservoir for ablation after its transfer to lattice atoms/ions, with T_e reaching ~2 keV in typical metal and silicon drilling [56]. The maximum of material removed by a single pulse can be estimated from energy conservation [55]: $V_{max} = (1 - R)E_p/(n_a E_{at}/N_a)$, where E_{at} [J/mol] is the molar enthalpy of atomization and N_A is the Avogadro constant. Also here, the low reflectivity maximises material removal facilitated by larger absorbance (Eq. 4), which is additionally enhanced due to p-pol. at a large angle of incidence at the laser pulse and side-walls of nano-needles $\theta_i \sim \theta_B \approx 75°$, where θ_B is the Brewster angle.

5. Conclusions and outlook

It is demonstrated that the anti-reflective surface of b-Si facilitates very precise energy deposition at the focal spot with a smooth transition from the ablation (removal of material via ionisation above 0.2 J/cm^2) to a well-controlled energy deposition and melting of the surface nanotexture at fluencies of 4 mJ/cm^2. The width of the molten -resolidified region closely follows the focal spot size. The reduction of ablation threshold by 50$^{\times}$ is related to the increased absorbance (reduced reflectance) of b-Si. Change of reflectance of Si vs b-Si $R/R_b = (1 - R_b)/(1 - R) \equiv A_b/A \approx 40\,\%/1\,\% \sim 40$. This factor of ablation threshold reduction is achievable due to optical properties and energy deposition into the very same Si (same binding energy and ionisation potential), governed by geometrical factors of the surface texture. It is noteworthy that an estimation of such a reduction factor of ablation threshold is only qualitative since the energy deposition is a dynamic fast process governed via free carrier (electron-hole) generation and self-action on the incoming light. The energy deposition is determined via the instantaneous complex permittivity ε^* of irradiated surface of b-Si. The condition when the real part of permittivity lies between 1 and 0 (a dielectric breakdown) is called the epsilon near zero (ENZ) [57] or die-met [58] state corresponding to strong absorption, phase changes of propagating/reflecting light [59], and localisation of light at nanoscale [60].

Further experimental efforts to explore the reduction of ablation thresholds due to the texture of the same material as the host substrate could open new methods for controlling resolution and feature size of the nanoscale energy deposition. The linear and nonlinear optical properties of nano-textured surfaces have contributing effects.

CRediT authorship contribution statement

Nan Zheng: Visualization, Validation, Investigation, Formal analysis, Data curation. **Hsin-Hui Huang:** Writing – original draft, Investigation, Data curation. **Nguyen Hoai An Le:** Visualization, Validation, Investigation. **Tomas Katkus:** Validation, Methodology, Investigation. **Haoran Mu:** Validation, Investigation, Data curation. **Soon Hock Ng:** Validation, Investigation, Data curation. **Thumula Ranaweera:** Validation, Investigation. **Darius Gailevičius:** Validation, Investigation, Data curation. **Dominyka Stonytė:** Visualization, Validation, Methodology, Investigation, Data curation, Conceptualization. **Saulius Juodkazis:** Writing – original draft, Validation, Conceptualization.

Declaration of competing interest

The authors declare that they have no known competing financial interests or personal relationships that could have appeared to influence the work reported in this paper.

Acknowledgement

This study was carried out via ARC DP240103231 grant. This work was performed on the fs-fab laser station at Swinburne, which is jointly funded with the Melbourne Centre for Nanofabrication (MCN), the

Victorian Node of the Australian National Fabrication Facility (ANFF). We thank Workshop-of-Photonics (WOP) Ltd., Lithuania for the patent license and technology transfer project through which the industrial fs-laser fabrication setup was acquired for Nanolab, Swinburne.

Data availability

Data will be made available on request.

References

[1] B. Franta, E. Mazur, S.K. Sundaram, Ultrafast laser processing of silicon for photovoltaics, Int. Mater. Rev. 63 (2018) 227–240.
[2] Y.-F. Huang, S. Chattopadhyay, Y.-J. Jen, C.-Y. Peng, T.-A. Liu, Y.-K. Hsu, C.-L. Pan, H.-C. Lo, C.-H. Hsu, Y.-H. Chang, C.-S. Lee, K.-H. Chen, L.-C. Chen, Improved broadband and quasi-omnidirectional anti-reflection properties with biomimetic silicon nanostructures, Nat. Nanotechnol. 2 (2007) 770–774, https://doi.org/10.1038/nnano.2007.389
[3] Y. Nishijima, R. Komatsu, S. Ota, G. Seniutinas, A. Balčytis, S. Juodkazis, Antireflective surfaces: cascading nano/microstructuring, APL Photonics 1 (2016) 076104, https://doi.org/10.1063/1.4964851
[4] Z. Fan, D. Cui, Z. Zhang, Z. Zhao, H. Chen, Y. Fan, P. Li, Z. Zhang, C. Xue, S. Yan, Recent progress of black silicon: from fabrications to applications, Nanomaterials 11 (2020) 41, https://doi.org/10.3390/nano11010041
[5] K.M. Eisele, SF 6, a preferable etchant for plasma etching silicon, J. Electrochem. Soc. 128 (1981) 123–126, https://doi.org/10.1149/1.2127351
[6] H. Jansen, M. De Boer, H. Wensink, B. Kloeck, M. Elwenspoek, The black silicon method. VIII. A study of the performance of etching silicon using SF6/O_2-based Chemistry with cryogenical wafer cooling and a high density ICP source, Microelectron. J. 32 (2001) 769–777, https://doi.org/10.1016/S0026-2692(01)00039-8
[7] V.T.H. Nguyen, F. Jensen, J. Hübner, P. Leussink, H. Jansen, On the formation of black silicon in SF6-O_2 plasma: the clear, oxidize, remove, and etch (CORE) sequence and black silicon on demand, J. Vac. Sci. Technol. A 38 (2020) 043004, https://doi.org/10.1116/6.0000196
[8] Y. Nishijima, H. Nishijima, M. Ohashi, T. Katkus, S. Juodkazis, Efficient water evaporation using black silicon, ACS Sustain. Resour. Manag. 2 (2025) 316–321, https://doi.org/10.1021/acssusresmgt.4c00418
[9] P. Ščajev, T. Malinauskas, G. Seniutinas, M. Arnold, A. Gentle, I. Aharonovich, G. Gervinskas, P. Michaux, J. Hartley, E. Mayes, P. Stoddart, S. Juodkazis, Light-induced reflectivity transients in black-si nanoneedles, Sol. Energy Mater. Sol. Cells 144 (2016) 221–227, https://doi.org/10.1016/j.solmat.2015.08.030
[10] M.-J. Sher, Y.-T. Lin, M.T. Winkler, B. Franta, E. Mazur, (Eds.) B. Di Bartolo J Collins, Femtosecond Laser Doped Silicon for Photovoltaic Applications, in Nano-Optics for Enhancing Light-Matter Interactions on a Molecular Scale, Springer, Netherlands, Dordrecht, 2013, p. 449.
[11] X. Liu, P.R. Coxon, M. Peters, B. Hoex, J.M. Cole, D.J. Fray, Black silicon: fabrication methods, properties and solar energy applications, Energy Environ. Sci. 7 (2014) 3223–3263, https://doi.org/10.1039/C4EE01152J
[12] R. Bilyalov, R. Lüdemann, W. Wettling, L. Stalmans, J. Poortmans, J. Nijs, L. Schirone, G. Sotgiu, S. Strehlke, C. Lévy-Clément, Multicrystalline silicon solar cells with porous silicon emitter, Sol. Energy Mater. Sol. Cells 60 (2000) 391–420, https://doi.org/10.1016/S0927-0248(99)00102-6
[13] R.J. Martín-Palma, L. Vázquez, J.M. Martínez-Duart, M. Schnell, S. Schaefer, Antireflective porous-silicon coatings for multicrystalline solar cells: the effects of chemical etching and rapid thermal processing, Semicond. Sci. Technol. 16 (2001) 657–661, https://doi.org/10.1088/0268-1242/16/8/303
[14] M. Saadoun, N. Mliki, H. Kaabi, K. Daoudi, B. Bessaıs, H. Ezzaouia, R. Bennaceur, Vapour-etching-based porous silicon: a new approach, Thin Solid Films. 405 (2002) 29–34, https://doi.org/10.1016/S0040-6090(01)01757-6
[15] H.-D. Um, N. Kim, K. Lee, I. Hwang, J.H. Seo, Y.J. Yu, P. Duane, M. Wober, K. Seo, Versatile control of metal-assisted chemical etching for vertical silicon microwire arrays and their photovoltaic applications, Sci. Rep. 5 (2015) 11277, https://doi.org/10.1038/srep11277
[16] C. Huo, J. Wang, H. Fu, X. Li, Y. Yang, H. Wang, A. Mateen, G. Farid, K.-Q. Peng, Metal-assisted chemical etching of silicon in oxidizing HF solutions: origin, mechanism, development, and black silicon solar cell application, Adv. Funct. Mater. 30 (2020) 2005744, https://doi.org/10.1002/adfm.202005744
[17] J. Soueiti, R. Sarieddine, H. Kadiri, A. Alhussein, G. Lerondel, R. Habchi, A review of cost-effective black silicon fabrication techniques and applications, Nanoscale 15 (2023) 4738–4761, https://doi.org/10.1039/D2NR06087F
[18] M. Halbwax, T. Sarnet, M.S. Ph. Delaporte, H. Etienne, F. Torregrosa, V. Vervisch, I. Perichaud, S. Martinuzzi, Micro and nano-structuration of silicon by femtosecond laser: application to silicon photovoltaic cells fabrication, Thin Solid Films. 516 (2008) 6791–6795, https://doi.org/10.1016/j.tsf.2007.12.117
[19] K. Nguyen, D. Abi-Saab, P. Basset, E. Richalot, F. Marty, D. Angelescu, Y. Leprince-Wang, T. Bourouina, Black silicon with sub-percent reflectivity: influence of the 3D texturization geometry, in: 2011 16th International Solid-State Sensors, Actuators and Microsystems Conference (IEEE, 2011, pp. 354–357.
[20] J. Oh, H.-C. Yuan, H.M. Branz, An 18.2 %-efficient black-silicon solar cell achieved through control of carrier recombination in nanostructures, Nat. Nanotechnol. 7 (2012) 743–748, https://doi.org/10.1038/nnano.2012.166
[21] M. Otto, M. Algasinger, H. Branz, B. Gesemann, T. Gimpel, K. Füchsel, T. Käsebier, S. Kontermann, S. Koynov, X. Li, V. Naumann, J. Oh, A.N. Sprafke, J. Ziegler, M. Zilk, R.B. Wehrspohn, Black silicon photovoltaics, Adv. Opt. Mater. 3 (2015) 147–164, https://doi.org/10.1002/adom.201400395
[22] J.-H. Chai, B. Wong, S. Juodkazis, Black-silicon-assisted photovoltaic cells for better conversion efficiencies: a review on recent research and development efforts, Mater. Today Energy 18 (2020) 100539, https://doi.org/10.1016/j.mtener.2020.100539
[23] J. Lv, T. Zhang, P. Zhang, Y. Zhao, S. Li, Review application of nanostructured black silicon, Nanoscale Res. Lett. 13 (2018) 110.
[24] Z. Zhao, Z. Zhang, J. Jing, R. Gao, Z. Liao, W. Zhang, G. Liu, Y. Wang, K. Wang, C. Xue, Black silicon for near-infrared and ultraviolet photodetection: a review, Materials 11 (2023) 021107, https://doi.org/10.1063/5.0133770APL
[25] Q. Tan, F. Lu, C. Xue, W. Zhang, L. Lin, J. Xiong, Nano-fabrication methods and novel applications of black silicon, sensors and actuators a, Physical 295 (2019) 560–573.
[26] E.P. Ivanova, J. Hasan, H.K. Webb, G. Gervinskas, S. Juodkazis, V.K. Truong, A.H. Wu, R.N. Lamb, V.A. Baulin, G.S. Watson, J.A. Watson, D.E. Mainwaring, R.J. Crawford, Bactericidal activity of black silicon, Nat. Commun. 4 (2013) 2838, https://doi.org/10.1038/ncomms3838
[27] M. Garcia-Lechuga, N. Casquero, J. Siegel, J. Solis, R. Clady, A. Wang, O. Utéza, D. Grojo, Amorphization and ablation of crystalline silicon using ultrafast lasers: dependencies on the pulse duration and irradiation wavelength, Laser Photonics Rev. 18 (2024) 2301327, https://doi.org/10.1002/lpor.202301327
[28] N.N. Greenwood, A. Earnshaw, Chemistry of the Elements, 2nd ed., Butterworth-Heinemann, Oxford Boston, 1997.
[29] R. Perkins, L. Geoffrion, J. Biery, Densities of Some Low Melting Plutonium Alloys (IAEA, Los Alamos National Lab(LANL), Los Alamos, NM (United States), 1966, pp. 473–491.
[30] R.A. Khairulin, S.V. Stankus, R.N. Abdullaev, V.M. Sklyarchuk, The density and interdiffusion coefficients of bismuth-tin melts of eutectic and near-eutectic composition, High Temp. 48 (2010) 188–191.
[31] W. Yang, J. Mathews, J. Williams, Hyperdoping of Si by ion implantation and pulsed laser melting, Adv. Doping Methods in Semicond. Devices and Nanostructures 62 (2017) 103–114, https://doi.org/10.1016/j.mssp.2016.11.005. Materials Science in Semiconductor Processing.
[32] C. Li, J.-H. Zhao, Z. Chen, Infrared absorption and sub-bandgap photo-response of hyperdoped silicon by ion implantation and ultrafast laser melting, J. Alloys Compd. 883 (2021) 160765, https://api.semanticscholar.org/CorpusID:236310660.
[33] Z. Tong, M. Bu, Y. Zhang, D. Yang, X. Pi, Hyperdoped silicon: processing, properties, and devices, J. Semicond. 43 (2022) 093101, https://doi.org/10.1088/1674-4926/43/9/093101
[34] J. Kaupuzs, P. Onufrijevs, P. Scajev, H.H. Cheng, G.-E. Chang, Y. Tsuchiya, Phase field calculations of SN redistribution in gesn/si structure after pulsed laser irradiation, Opt. Laser Technol. 189 (2025) 113046.
[35] S. Pandolfi, S.B. Brown, P.G. Stubley, A. Higginbotham, C.A. Bolme, H.J. Lee, B. Nagler, E. Galtier, R.L. Sandberg, W. Yang, W.L. Mao, J.S. Wark, A.E. Gleason, Atomistic deformation mechanism of silicon under laser-driven shock compression, Nat. Commun. 13 (2022) 5535.
[36] L. Rapp, B. Haberl, C. Pickard, J. Bradby, E. Gamaly, J. Williams, A. Rode, Experimental evidence of new tetragonal polymorphs of silicon formed through ultrafast laser-induced confined microexplosion, Nat. Commun. 6 (2015) 7555.
[37] R.L. Nowack, A tale of two beams: an elementary overview of Gaussian beams and Bessel beams, Stud. Geophys. Geod. 56 (2012) 355–372, https://doi.org/10.1007/s11200-011-9054-0
[38] M. Duocastella, C. Arnold, Bessel and annular beams for materials processing, Laser Photon. Rev. 6 (2012) 607–621, https://doi.org/10.1002/lpor.201100031
[39] R. Stoian, M.K. Bhuyan, G. Zhang, G. Cheng, R. Meyer, F. Courvoisier, Ultrafast Bessel beams: advanced tools for laser materials processing, Adv. Opt. Technol. 7 (2018) 165–174, https://doi.org/10.1515/aot-2018-0009
[40] A.S. Rao, A conceptual review on Bessel beams, Phys. Scr. 99 (2024) 062007, https://doi.org/10.1088/1402-4896/ad4921.
[41] M.K. Bhuyan, F. Courvoisier, P.A. Lacourt, M. Jacquot, R. Salut, L. Furfaro, J.M. Dudley, High aspect ratio nanochannel machining using single shot femtosecond bessel beams, Appl. Phys. Lett. 97 (2010) 081102, https://doi.org/10.1063/1.3479419
[42] A. Mathis, F. Courvoisier, L. Froehly, L. Furfaro, M. Jacquot, P.A. Lacourt, J.M. Dudley, Micromachining along a curve: femtosecond laser micromachining of curved profiles in diamond and silicon using accelerating beams, Appl. Phys. Lett. 101 (2012) 071110, https://doi.org/10.1063/1.4745925
[43] A. Marcinkevičius, S. Juodkazis, S. Matsuo, V. Mizeikis, H. Misawa, Application of bessel beams for microfabrication of dielectrics by femtosecond laser, Jpn. J. Appl. Phys. 40 (2001) L1197, https://doi.org/10.1143/JJAP.40.L1197
[44] S.N. Khonina, N.L. Kazanskiy, P.A. Khorin, M.A. Butt, Modern types of axicons: new functions and applications, Sensors 21 (2021) https://doi.org/10.3390/s21196690Sensors
[45] R. Dharmavarapu, S. Bhattacharya, S. Juodkazis, Diffractive Optics for axial intensity shaping of bessel beams, J. Opt. 20 (2018) 085606, https://doi.org/10.1088/2040-8986/aad155
[46] J. Bonse, S. Baudach, J. Krūger, W. Kautek, M. Lenzner, Femtosecond laser ablation of silicon–modification thresholds and morphology, Appl. Phys. A 74 (2002) 19–25.
[47] J.M. Liu, Simple technique for measurements of pulsed gaussian-beam spot sizes, Opt. Lett. 7 (1982) 196–198, https://doi.org/10.1364/OL.7.000196
[48] V.V. Belloni, L. Froehly, C. Billet, L. Furfaro, F. Courvoisier, Generation of extremely high-angle bessel beams, Appl. Opt. 62 (2023) 1765–1768, https://doi.org/10.1364/AO.482826.
[49] R. Herman, T. Wiggins, Production and uses of diffractionless beams, J. Opt. Soc. Am. A 8 (1991) 932–942.
[50] V. Anand, J. Maksimovic, T. Katkus, S.H. Ng, O. Ulčinas, M. Mikutis, J. Baltrukonis, A. Urbas, G. Šlekys, H. Ogura, D. Sagae, T. Pikuz, T. Somekawa, N. Ozaki,

A. Vailionis, G. Seniutinas, V. Mizeikis, K. Glazebrook, J.P. Brodie, P.R. Stoddart, L. Rapp, A.V. Rode, E.G. Gamaly, S. Juodkazis, All femtosecond optical pump and x-ray probe: holey-axicon for free electron lasers, J. Phys.: Photonics 3 (2021) 024002, https://doi.org/10.1088/2515-7647/abd4ef

[51] T. Katkus, S.H. Ng, H. Mu, N.H.A. Le, D. Stonytė, Z. Khajehsaeidimahabadi, G. Seniutinas, J. Baltrukonis, O. Ulcinas, M. Mikutis, V. Sabonis, Y. Nishijima, M. Rienäcker, U. Römer, J. Krügener, R. Peibst, S. John, S. Juodkazis, Bessel-beam direct write of the etch mask in a nano-film of alumina for high-efficiency SI solar cells, Adv. Eng. Mater. 26 (2024) 2400711, https://doi.org/10.1002/adem.202400711

[52] M. Garcia-Lechuga, D. Grojo, Simple and robust method for determination of laser fluence thresholds for material modifications: an extension of liu's approach to imperfect beams, Open Res Europe 1 (7) (2021).

[53] J. Fu, D. Yang, X. Yu, Hyperdoped crystalline silicon for infrared photodetectors by pulsed laser melting: a review, Phys. Status Solidi A 219 (2022) 2100772, https://doi.org/10.1002/pssa.202100772.

[54] D.P. Linklater, F. Haydous, C. Xi, D. Pergolesi, J. Hu, E.P. Ivanova, S. Juodkazis, T. Lippert, J. Juodkazytė, Black-si as a photoelectrode, Nanomaterials 10 (2020) https://doi.org/10.3390/nano10050873

[55] E.G. Gamaly, A.V. Rode, B. Luther-Davies, Ablation of solids by femtosecond lasers: ablation mechanism and ablation thresholds for metals and dielectrics, Phys. Plasmas 18 (2002) 949–957.

[56] S. Juodkazis, H. Okuno, N. Kujime, S. Matsuo, H. Misawa, Hole drilling in stainless steel and silicon by femtosecond pulses at low pressure, Appl. Phys. A 79 (2004) 1555–1559, https://doi.org/10.1007/s00339-004-2846-0

[57] J.B. Khurgin, M. Clerici, N. Kinsey, Fast and slow nonlinearities in epsilon-near-zero materials, Laser Photon. Rev. 15 (2021) 2000291, https://doi.org/10.1002/lpor.202000291, https://arxiv.org/abs/https://onlinelibrary.wiley.com/doi/pdf/10.1002/lpor.202000291.

[58] E.G. Gamaly, A.V. Rode, Ultrafast re-structuring of the electronic landscape of transparent dielectrics: new material states (die-met), Appl. Phys. A 124 (2018) 278.

[59] S. Juodkazis, K. Nishimura, H. Misawa, Three-dimensional laser structuring of materials at tight focusing, Chin. Opt. Lett. 5 (2007) S198.

[60] Z.-Z. Li, H. Fan, L. Wang, X. Zhang, X.-J. Zhao, Y.-H. Yu, Y.-S. Xu, Y. Wang, X.-J. Wang, S. Juodkazis, Q.-D. Chen, H.-B. Sun, Super-stealth dicing of transparent solids with nanometric precision, Nat. Photonics 18 (2024) 799–808.